IOP Publishing Journal of Physics: Condensed Matter
J. Phys.: Condens. Matter **33** (2021) 215803 (9pp) https://doi.org/10.1088/1361-648X/abe64c

Theoretical study of tunable magnetism of two-dimensional $MnSe_2$ through strain, charge, and defect

Wen-Qiang Xie[1], Zhi-Wei Lu[1], Chang-Chun He[1], Xiao-Bao Yang[1,2] and Yu-Jun Zhao[1,2,*]

[1] Department of Physics, South China University of Technology, Guangzhou 510640, People's Republic of China
[2] Key Laboratory of Advanced Energy Storage Materials of Guangdong Province, South China University of Technology, Guangzhou 510640, People's Republic of China, Tel: +86-20-87110426; Fax: +86-20-87112837

E-mail: zhaoyj@scut.edu.cn

Received 14 November 2020, revised 31 January 2021
Accepted for publication 15 February 2021
Published 29 April 2021

Abstract

Two-dimensional transition metal dichalcogenide $MnSe_2$ (2D-$MnSe_2$) with Curie temperature approximate to 300 K has a significant spintronic application on thin-film devices. We demonstrate theoretically a tunable magnetic transition of 2D-$MnSe_2$ between anti-ferromagnetic (AFM) metal and ferromagnetic (FM) half metal as strain increasing. Mechanism of that transition involves a competition between d–p–d through-bond and d–d direct interaction in 2D-$MnSe_2$. Hole doping is an alternative way to enhance the stability of FM coupling. Adsorption (including Li, Na, Cl and F) and vacancy (Mn and Se) studies confirm that the controllable magnetism of 2D-$MnSe_2$ is related to both interaction competition and charge doping. Tensile strains can greatly amplify through-bond interaction and exchange parameters, resulting in a sharp increase of Curie temperature.

Keywords: two-dimensional $MnSe_2$, tunable magnetism, Curie temperature, magnetic orientation, first-principles calculation

S Supplementary material for this article is available online

(Some figures may appear in colour only in the online journal)

1. Introduction

Past decades have witnessed tremendous efforts of exploring two-dimensional (2D) materials, including graphene [1], boron nitride sheet [2], black phosphorus [3] etc, which own many fascinating electronic properties like strong ambipolar electric field effect [4] and integer quantum Hall effect [5]. Moreover, magnetic 2D materials with controllable magnetism are crucial for designing spintronics and valleytronics heterostructure [6]. For example, magneto-elastic coupling [7] and electrical tuning [8] of atomic thickness materials, provide unique opportunities to control their magnetic properties. It thus has opened up the prospect of the realization of new functional devices [9].

Enormous attention has gained in studying the magnetism of 2D materials these days, such as Fe_3GeTe_2 [10, 11], CrI_3 [12, 13] and transition metal dichalcogenide monolayers [14]. Experimentally, 2D Fe_3GeTe_2 has been synthesized with the Curie temperature of about 205 K [15], but most of the 2D materials can only exhibit ferromagnetism with Curie temperature around 40 K and below [11, 16–18], seriously limiting their application in practical spintronic applications. Exploring 2D magnetic materials with high Curie temperature is accessible and of great interest. Interestingly, O'Hara [6] synthesized a room temperature ferromagnetic (FM) 2D-$MnSe_2$, imply-

* Author to whom any correspondence should be addressed.

ing exciting application for nano-scale spintronic devices, such as energy-efficient information storage device. Additionally, $MnSe_2$ with high-performance electronic properties is widely used as electrode material [19, 20]. Therefore, combining its unique electronic and magnetic properties with atomic thickness, 2D-$MnSe_2$ could exhibit a great potential value for nanometer-scale functional devices. Nevertheless, strains, adsorption and vacancies may be accompanied when $MnSe_2$ is employed for 2D devices. For example, most 2D monolayers are produced via chemical vapour deposition (CVD) method [6, 21, 22]. Based on different substrates, the produced monolayer might be imposed with strain, adsorption and defect on its surface. On the other hand, strain [23], adsorption [24], and defect [25] are the most natural and feasible methods to manipulate the properties of materials in experiments. Therefore, investigating the effects of these factors towards its electronic and magnetic properties are of interest for practical applications.

In this work, via strains, charge, adsorptions and vacancies, we extensively explore the possibility of controlling the magnetic properties of 2D-$MnSe_2$, unveiling the influence of d–p–d through-bond and d–d direct interaction competition, as well as the charge doping towards intrinsic magnetic properties of 2D-$MnSe_2$. Further, we have estimated the exchange parameters and magnetocrystalline anisotropy energy (MAE) to evaluate the impacts of these approaches on improving 2D-$MnSe_2$'s Curie temperature, for potential magneto-elastic application of 2D-$MnSe_2$.

2. Computational details

The calculations are conducted based on the density functional theory [26, 27], by using the Vienna *ab initio* simulation package (VASP) [28] code. The projector augmented-wave [29] method is employed with the Perdew–Burke–Ernzerhof (PBE) [30] type generalized gradient approximation (GGA) for describing the exchange–correlation potential. To properly describe the strong correlated electrons in the partially filled d subshells, GGA + U_{eff} is introduced with $U_{\text{eff}} = 3.9$ eV for Mn atom, as reported in earlier studies [14, 31–33]. The HSE06 [34] hybrid functional and Hartree–Fock [35] method are used for calculating the band structure accurately. The cutoff energy of 400 eV for the plane waves basis set is adopted. To avoid interactions between two neighbour images, the vacuum layer is set to 15 Å. The reciprocal space integrations are sampled with Gamma centred meshes following the Monkhorst–Pack method [36], with $12 \times 12 \times 1$, $8 \times 8 \times 1$ and $4 \times 8 \times 1$ for primitive cell, $(2 \times 2 \times 1)$ and $(4 \times 2 \times 1)$ supercell, respectively. The phonon dispersion relations are calculated via PHONOPY code [37] with a $(3 \times 3 \times 1)$ supercell. For magnetic anisotropy energy (MAE) calculation, we apply $16 \times 16 \times 1$ mesh for $(2 \times 2 \times 1)$ supercell to ensure the accuracy, with the spin–orbit coupling taken into account. Curie temperature was simulated by Vampire [38], in which the 2D-$MnSe_2$ was extended to a (30 nm × 30 nm) monolayer to induce periodic constraints. Also, 3×10^5 equilibration steps and 2×10^5 loop steps are taken to achieve an average magnetic moment value.

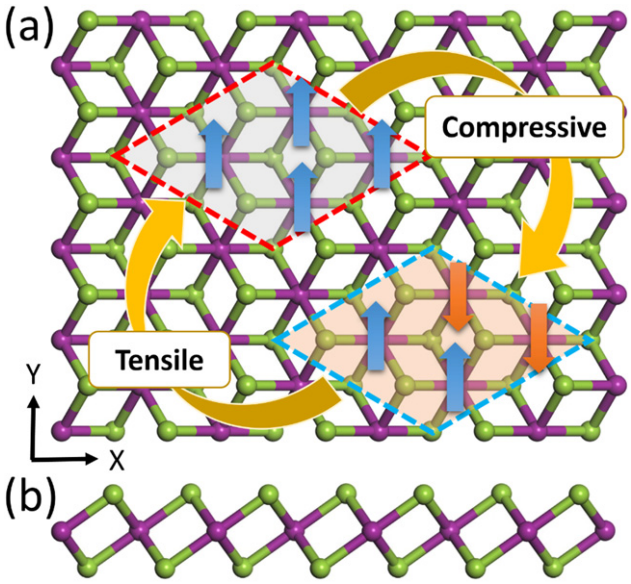

Figure 1. (a) Top view and (b) side view geometry of 2D-$MnSe_2$ where Mn atoms are purple and Se atoms are green. The red and blue dash-line rhombus indicate FM and AFM configuration, respectively. Employing tensile or compressive strain can lead to a transition between FM and AFM configuration.

The energy difference between FM and anti-ferromagnetic (AFM) is defined by:

$$\Delta E = E_{\text{AFM}} - E_{\text{FM}},$$

here, E_{AFM} represents the energy of AFM 2D-$MnSe_2$ and E_{FM} the FM 2D-$MnSe_2$. Angular (θ) dependence of the (MAE(θ)) in $xy-$, $yz-$ and $xz-$ planes have been defined as below:

$$\text{MAE}(\theta) = E_\theta - E_0,$$

where E_θ and E_0 are the energies of magnetic configurations with the spin vector of S_θ and S_0 in the same plane. Spin vector S_θ is rotated with an angle of θ about S_0.

3. Results and discussion

3.1. Strain-induced magnetic transition and interactive competition between d–p–d through-bond and d–d direct interaction

The geometric structure of 2D-$MnSe_2$ is depicted in figure 1, where Mn atoms bonded to Se atoms is in an octahedral configuration. To validate various properties from the theoretical calculations, the structural details of 2D-$MnSe_2$ with different exchange–correlation functionals from available literature are listed in table S1 (https://stacks.iop.org/JPCM/33/215803/mmedia). Comparing with results from other functionals, PBE + U_{eff} presents the maximum lattice parameters and the maximum magnetic moment of Mn (M_{Mn}), with the corresponding values of 3.65 Å and 3.95 μ_{B}, respectively. These values are in agreement with previous predictions [14, 39], but smaller than O'Hara's experimental observation [6] by 0.25 Å and 0.45 μ_{B}, respectively. This discrepancy may attribute to the experimental

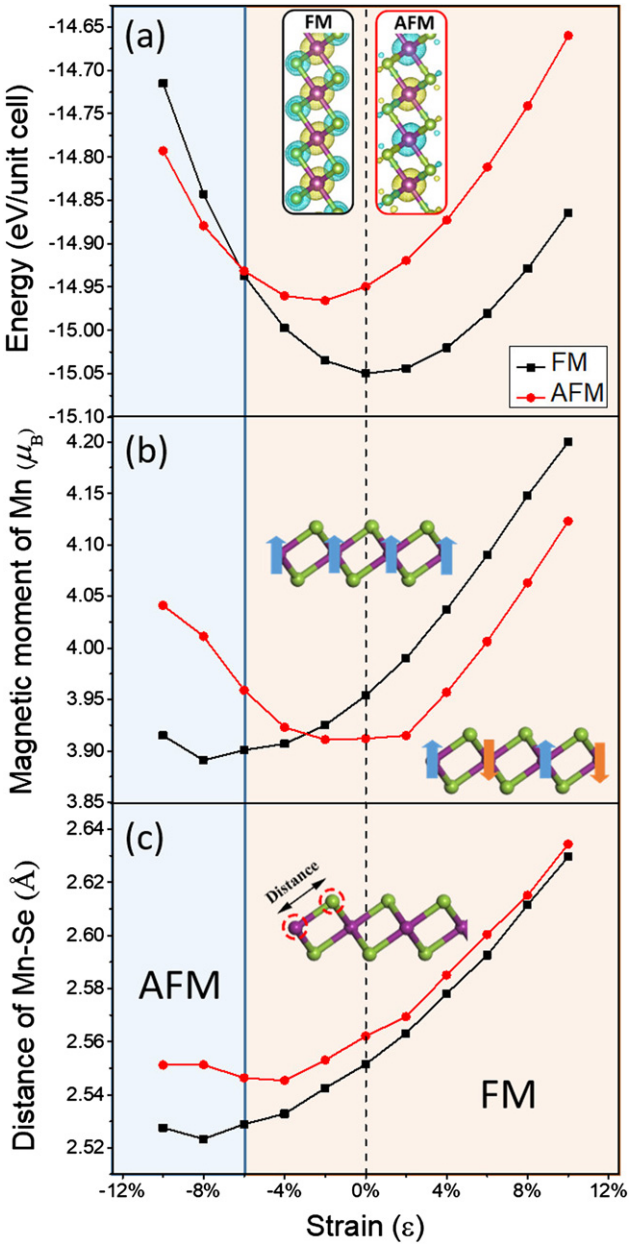

Figure 2. (a) The energy of FM and AFM 2D-$MnSe_2$ under various strains; insert: spin density of FM and AFM configurations. The blue and yellow spheres indicate down and up spin, respectively. The isosurfaces are set as 0.01 eV $Å^{-3}$. (b) Magnetic moments of Mn in FM and AFM under various strains. (c) The distance of Mn–Se bond in FM and AFM under various strains. Here the blue region (strain $< -6\%$) indicates the AFM coupling favour, and the pink region (strain $> -6\%$) indicates the FM coupling favour.

preparation method of CVD, where 2D-$MnSe_2$ was grown on the GaSe substrate. Substrates could exert remarkable influence on 2D-$MnSe_2$ monolayer, such as tensile or compressive strains, charges, etc. Actually, 2D materials and its critical magnetic properties [40, 41], would be easily affected by these factors.

Our systematical studies start from the impact of biaxial strains on the magnetic couplings of 2D-$MnSe_2$ (cf figure 1). The biaxial strain is defined as $\varepsilon = \Delta c/c_0$, where c_0 is the lattice parameter. The phonon dispersion relations of 2D-$MnSe_2$ under -8%, 0% and 8% strains show no imaginary frequencies (figure S1). Although phonon dispersion cannot exclude the possibility of buckling, it provides evidence of the kinetic stability of 2D-$MnSe_2$ under the strains [42]. As shown in figure 2(a), the tensile strains (strains form 0% to 10%) on 2D-$MnSe_2$ can enlarge the energy difference (ΔE) between FM and AFM, implying the enhanced stability of FM coupling. Nevertheless, compressing 2D-$MnSe_2$ (strains from 0% to -6%) could lead to the opposite trend. When the compressive strain is at -6%, a transition from FM to AFM phase occurs as illustrated in figure 2(a). Moreover, magnetic moment evolution in figure 2(b) also coincides with that magnetic transition. M_{Mn} of FM 2D-$MnSe_2$ decreases with the increment of compressive strains from -4% to -10%. But for AFM 2D-$MnSe_2$, M_{Mn} of AFM boosts sharply at that compressive strain range, indicating a magnetic transition (FM and AFM transition) occurs as we discussed above. The implementation of large strain in the experiment is still a challenge [43, 44], however, theoretical researches of the impact of large strains on the 2D materials can give us some significant insight and possible approaches to tune their properties [45–47]. Besides biaxial strains, we have also conducted simulations of uniaxial strain on 2D-$MnSe_2$ to figure out its impact. Due to the $P-3m1$ (164) symmetry of monolayer $MnSe_2$, we only consider the uniaxial strain along with one of the lattice vector. Similar to the biaxial strain, the energy difference between FM and AFM coupling keeps shrinking as strain decreases from 10% to -10% (figure S2(a)) and M_{Mn} of AFM increase as trains var form -4% to -10% (figure S2(b)). However, the magnetic transition is not induced by uniaxial strain.

The magnetic transition induced by biaxial strains may be ascribed to the competition between through-bond interaction and direct interaction [48]. Direct interaction implies that Mn atom with up-spin (down-spin) density induces an opposite magnetic density on the nearest Mn atom directly, without mediated by other atoms (see the AFM spin density in figure 2(a), insert). Since the spin density of Mn atoms is mainly contributed by its d orbit, thus direct interaction is a d–d orbit interaction. While through-bond interaction is Mn atom with up-spin (down-spin) density induces an opposite density on the adjacent Se atom bonded to it (see FM spin density in figure 2(a), insert), which may lead to FM spin coupling even in a long range. Because of the Se medium, through-bond interaction is a d–p–d orbit interaction. Based on this mechanism, we can also understand the evolution of the magnetic properties of AFM and FM with various strains. FM coupling is dominated by d–p–d through-bond interaction, implying that the adjacent Se atom is of significance to its magnetic properties. Compressing FM 2D-$MnSe_2$ would shorten the distance between Mn and Se atoms (d_{Mn-Se} in figure 2(c)), and lead to a strong Mn–Se covalent bond (a hybridized region in figure S3). This covalent bond will degrade the magnetic moments of Mn ions [49, 50] and reduce the effect of d–p–d through-bond interaction. However, for direct interaction dominated AFM, compressive strains form -4 % to -10 % somewhat increase the d_{Mn-Se} (figure 2(c)). It indicates an 'unlock' of M_{Mn}. Meanwhile, the shortened distance of Mn and adjacent Mn atoms (d_{Mn-Mn}) does not form a hybridized region

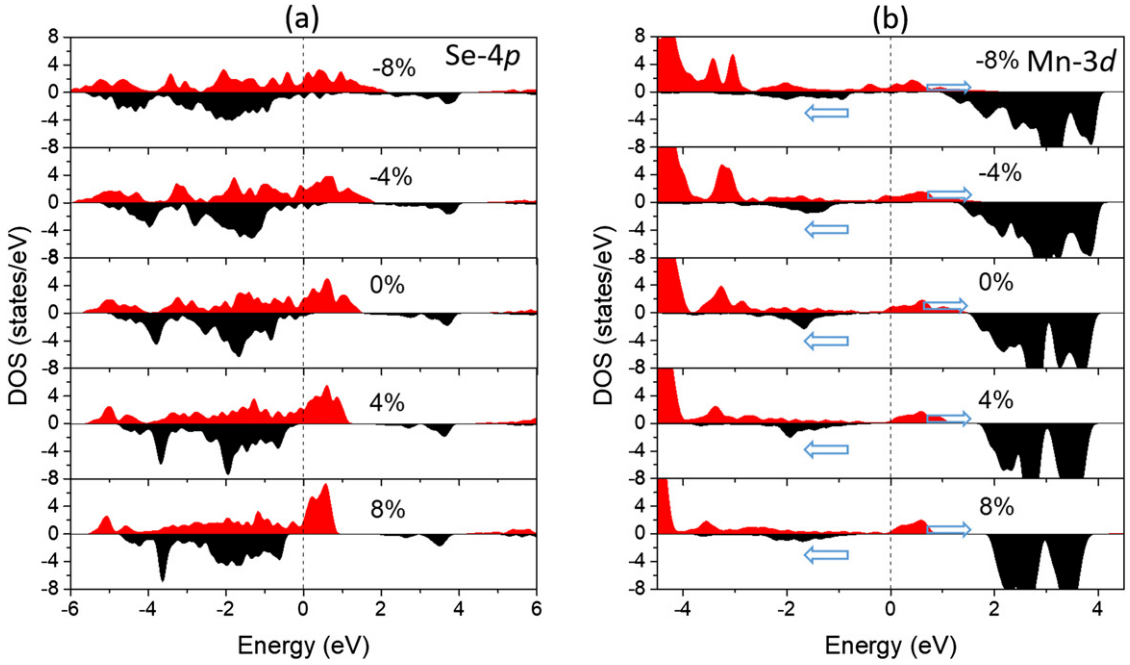

Figure 3. Se-4p (a) and Mn-3d (b) spin-polarized partial DOS of FM 2D-$MnSe_2$ under -8%, -4%, 0%, 4%, 8% biaxial strains. The red and black areas represent the spin-up and spin-down components, respectively, where the Fermi level is indicated by the dashed line. Blue arrows in (b) indicate spin splitting.

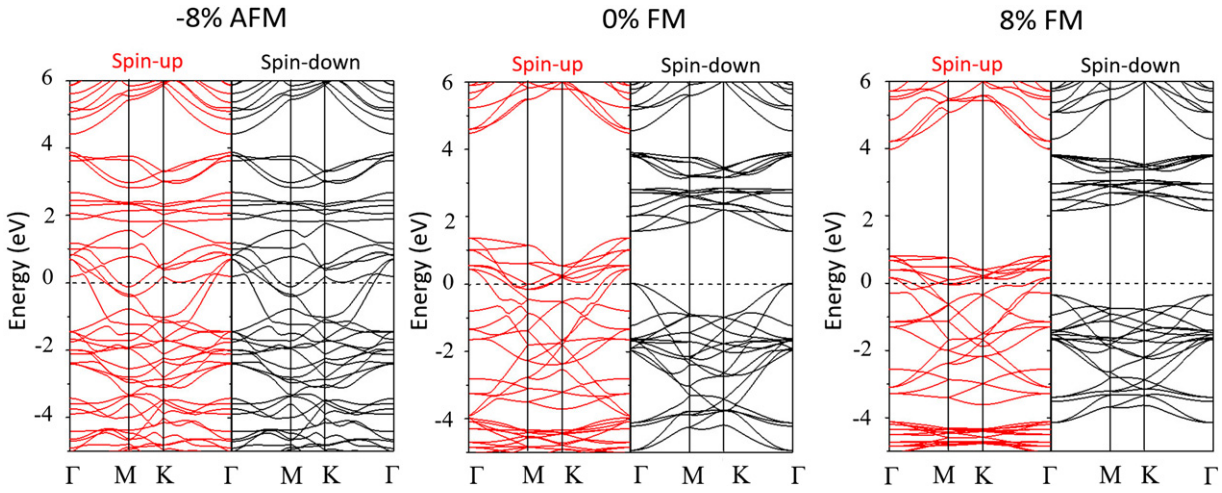

Figure 4. Spin-polarized band structures of 2D-$MnSe_2$ under -8%, 0%, 8% biaxial strain calculated by PBE + U_{eff}. The red and black lines represent the spin-up and spin-down components, respectively, where the Fermi level is indicated by the dashed line.

between them, and thus the intensity of d–d direct interaction will not be reduced. Instead of it, according to figure 2(a), d–d direct interaction is even amplified due to the shortened distance of $d_{\text{Mn–Mn}}$. As a result, both interactions exit in monolayer $MnSe_2$ and keep competing while strain is imposed. When the biaxial strain is beyond -6%, 2D-$MnSe_2$ prefers a through-bond FM interaction. When the biaxial strain less than -6%, however, it favours a direct AFM interactions.

This mechanism is also supported by its spin-polarized partial density states (DOS) of FM under -8%, -4%, 0%, 4% and 8% strains in figure 3. Near the Fermi level, the Se 4p states (figure 3(a)) in the 2D-$MnSe_2$ decrease at certain degree with the increase of tensile strain, indicating a reduction of hybridized interaction with Se atom. As a result, the exchange splitting of Mn 3d states may be unlocked. Meanwhile, the hybridized states of -4.5 to -0.3 eV (figure 3(b)) in the Mn-3d display a remarkable decrease as strain increasing, further confirming our above discussion. Spin polarization states near the Fermi level, highlighted by blue arrows in figure 3(b), translate into a perturbation for the polarized atom. It ends up enhancing the splitting effect and leads to an enhancement of magnetic moment [50]. The DOS of AFM configuration is shown in figure S4, also indicating a reduction of hybridized interaction between Mn and Se atom. Nevertheless, the sharp increase of M_{Mn} while compressing AFM 2D-$MnSe_2$ (figure 2(b), strains from -4 to -8%) is mainly ascribed to the reduced $d_{\text{Mn–Mn}}$

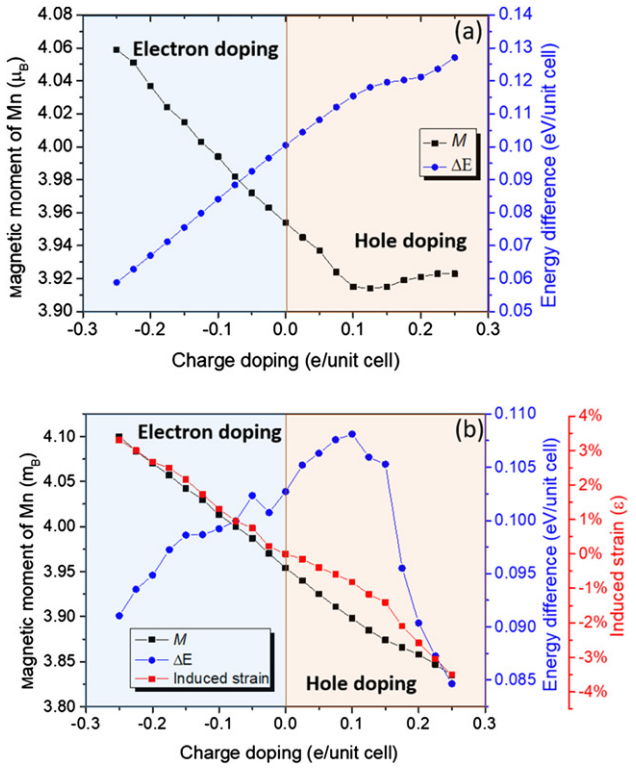

Figure 5. The evolution of magnetic moment (FM coupling Mn), ΔE, and the induced strains under various charge doping. (a) Lattice parameters are fixed; (b) lattice parameters are relaxed. FM and AFM coupling models for ΔE calculation are as depicted as figure 1. Here the blue region indicates electron doping, and the pink region indicates hole doping.

and the consequent enhancement of spin coupling [48, 51, 52]. Furthermore, while compressing AFM 2D-$MnSe_2$, this rapid increment of spin coupling may give rise to a magnetic transition.

3.2. Strain-induced evolution of band structures

Investigating the evolution of band structure under various strains is significant to unveil its electronic property. Figure 4 presents the spin-polarized band structures of 2D-$MnSe_2$ under -8%, 0% and 8% biaxial strains calculated by PBE + U_{eff}. When compressive strain is at -8%, the band structure exhibits a typical metal character as both spin-up and spin-down channels cross Fermi level. Without strain, the spin-down channel splits up and produces a gap, while spin-up one is crossing Fermi level, indicating a transition between metal and half-metal. As the strain approaches 8%, both channels keep moving upwards, but the spin-up channel still crosses the Fermi level. Similar results are also observed in HSE06 and Hartree–Fock band structures calculations (figure S5(a) and (b)). At zero strain, however, the HSE06 and Hartree–Fock band structures show a bit of difference compared to PBE + U_{eff}. At Γ point, the valence band maximums of both HSE06 and Hartree–Fock spin-down channel locate below Fermi level, while the maximum of PBE + U_{eff} locates at Fermi level. Regardless of this discrepancy, PBE + U_{eff}, HSE06 and Hartree–Fock band structures all present the same trend of the band structure evolution, i.e. 2D-$MnSe_2$ would go through a transition from AFM metal to FM half metal as strain increasing.

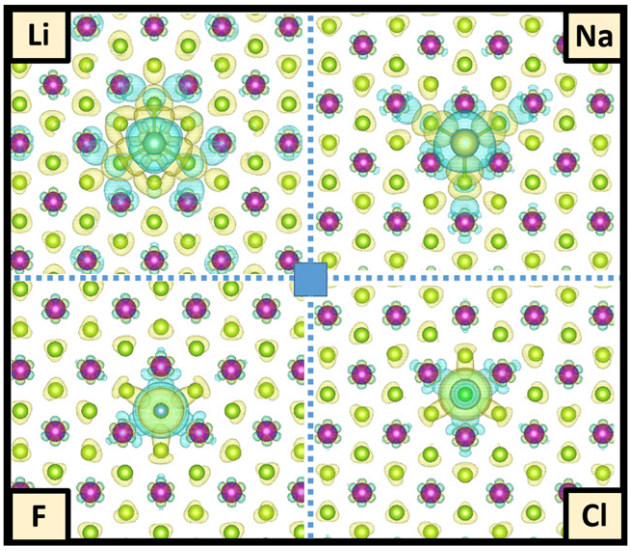

Figure 6. Charge density difference of Li–$MnSe_2$, Na–$MnSe_2$, F–$MnSe_2$ and Cl–$MnSe_2$, respectively. Yellow areas indicate regions of charge gain and blue areas indicate regions of charge loss. The isosurfaces were set to 0.015 eV $Å^{-3}$.

3.3. Effect of charge doping, adsorption and vacancies on 2D-$MnSe_2$'s magnetic properties

Charge doping is a feasible way to tune the properties of the system [53]. Through first-principles calculation, we find that the hole doping can lead to a decrease of M_{Mn}, while electron doping can lead to an increase (figures 5(a) and (b)). Noticeably, when the lattice parameters are fixed (figure 5(a)), ΔE of 2D-$MnSe_2$ exhibits a constant increase from 0.07 to 0.13 eV/unit cell as charge doping dosage ranges from -0.25 to 0.25 eV/unit cell. But when the lattice parameters are relaxed (figure 5(b)), ΔE shows a maximum value of 0.107 eV/unit cell with the hole doping amount of 0.08 eV/unit cell. Furthermore, figure 5(b) also indicates that electron doping can induce an uniform tensile strain in 2D-$MnSe_2$ while hole doping can introduce a compressive strain. The induced strain can up to $\pm 3\%$ with the charge doping dosage of ± 0.25 eV/unit cell. Therefore, the decrease of ΔE may ascribe to the hole doping induced compressive strain. Experimentally, charge doping can be realized by adsorption. We have calculated the adsorption of Cl, F, Li and Na atoms on the surface of 2D-$MnSe_2$, observing the changes of its magnetic coupling. There are three typical adsorption sites considered in the calculation (illustrated in figure S6). We find Li prefers to locate at site_1, on the top of Mn. Na locates at site_3, at the hollow of the 2D-$MnSe_2$ monolayer. F and Cl prefer at site_2, on the top of Se atom. The adsorption coverage is about 2%, and the lattice parameters are fixed in our simulation. Adsorption energies (E_a) for Li, Na, Cl and F atoms are as table S2. The magnitude of adsorption energy of F and Li are clearly greater than Cl and Na, indicating F and Li bind with $MnSe_2$ more stronger.

A minor increase in M_{Mn} is observed (see table S2) while Li and Na atoms are adsorbed. It may due to the electronic doping effect of these atoms (figure 5(a)). In addition to this, we also discover that a decrease of ΔE by about 10 meV per unit cell after Li and Na adsorptions. This phenomenon can be explained by electron doping (figure 5(a)) and the weakened d–p–d interaction. Form figure 6, charge density differences of Li–$MnSe_2$, Na–$MnSe_2$ reflect a strong interaction between the adsorbed atoms and the nearest three Se ions. The magnetic moment of the nearest three Se (M_{Se}) decreases by about 0.1 μ_B per Se ion. It confirms our earlier discussion that adsorbing Na and Li would weaken the d–p–d interaction. For Cl and F atoms, they are on the top of Se atom, figure 6 shows an interaction between adsorbing atoms and near Se. Although the regions of Cl–$MnSe_2$, F–$MnSe_2$ are smaller than Li–$MnSe_2$, Na–$MnSe_2$, it could also lead to a reduction the d–p–d interaction at a certain degree. Thus, ΔE of Cl–$MnSe_2$ and F–$MnSe_2$ are decreased by about 5 meV, significantly smaller than Li–$MnSe_2$ or Na–$MnSe_2$. Note that, adsorption of Cl and F atoms, will shorten the distance of Mn–Mn atoms (d_{Mn-Mn}) nearest to the adsorption sites by about 0.1 Å. This could also help to improve the direct interaction and M_{Mn}.

Vacancies in materials are sometimes critical to the properties of transition metal dichalcogenide [54, 55]. Eren's recent calculation [39] indicates that, even under the presence of high-density Se vacancies, 2D-$MnSe_2$ still preserves its dynamical stability. Therefore, we have investigated the impacts of Se and Mn vacancies on the properties of 2D-$MnSe_2$. To obtain ΔE for both Mn and Se vacancies. We adopt a ($5 \times 5 \times 1$) supercell for Mn vacancy calculation and a ($6 \times 6 \times 1$) supercell for Se vacancy calculation. The formation energies (ΔH) of Mn and Se vacancy with different synthesized environment are shown in figure S7. ΔH of Se vacancy is smaller than that of Mn vacancy as the chemical potential of Mn ranges from -1.6 to 0 eV, implying that forming Se vacancy is easier than Mn one. Se vacancy stripped the hybridized interaction between Se and Mn atoms, leading to 'unlock' M_{Mn}, and at the same time, it strongly weakens the d–p–d through-bond interaction. The deformation of spin density (figure S8) of the nearest Mn atom indicates the change of M_{Mn}, which reaches to the value of 4.17 μ_B. It is much approximately to the experiment one [6]. After introducing Se vacancy, ΔE is about 21 meV per unit cell smaller than the pristine one. Table S3 indicates Mn vacancy would bring down M_{Mn} of nearest Mn atoms to 3.85 μ_B. After introducing Mn vacancy, the ΔE of the system increases to 102.03 meV per unit cell. The introduction of Mn vacancy would give rise to an enhancement of d–p–d through-bond interaction. This result is in line with our above observation. In short, adsorption and vacancy controls offer valuable methods to tune the magnetic properties of 2D-$MnSe_2$. It confirms the critical impacts of interaction competition and charge doping on the magnetic properties of 2D-$MnSe_2$. It is significant for magnetic device application.

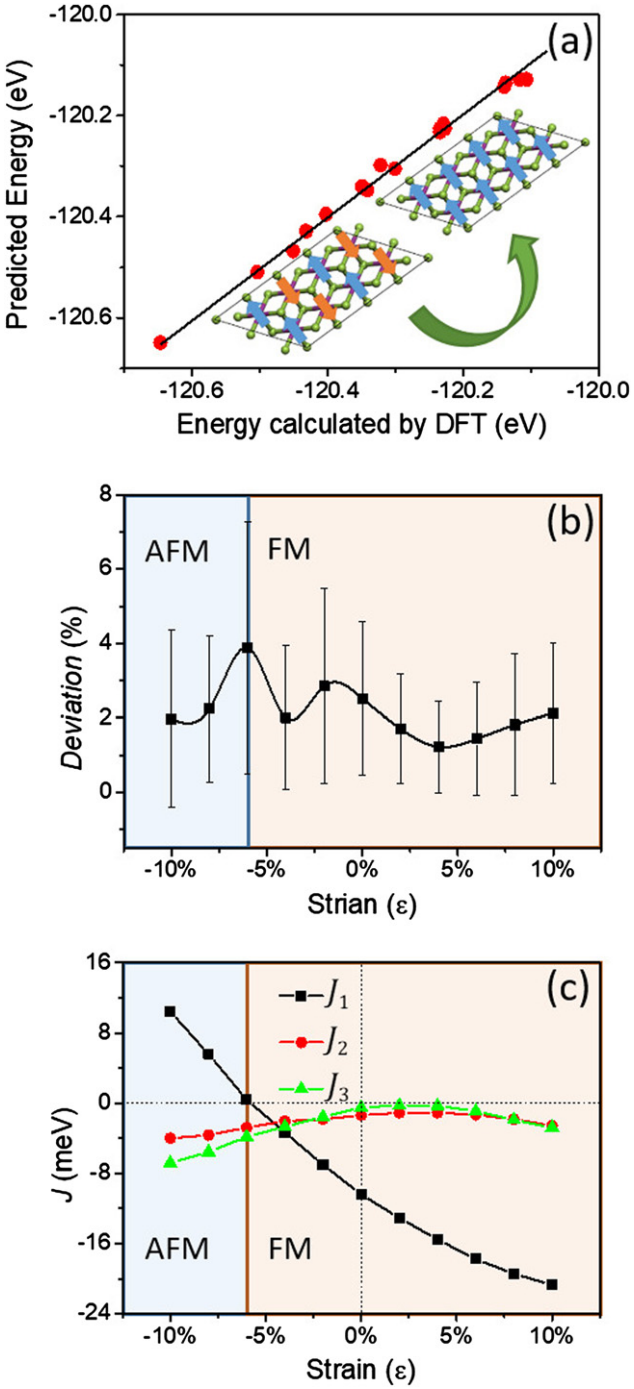

Figure 7. (a) The energy of 2D-$MnSe_2$ calculated by DFT and predicted by Heisenberg model under 0% strain. (b) The average deviation with error bars of Hamiltonian under various strains and (c) predicted Heisenberg exchange parameters.

3.4. Heisenberg model simulation, Curie temperature and MAE study of 2D-$MnSe_2$

To investigate the mechanism of magnetic transition induced by strain in detail, three-neighbour Heisenberg model Hamiltonian was applied. Its Hamiltonian is written as below:

$$H = \sum_{nn}^{n} J_1 S_i S_j + \sum_{2nn}^{n} J_2 S_i S_j + \sum_{3nn}^{n} J_3 S_i S_j,$$

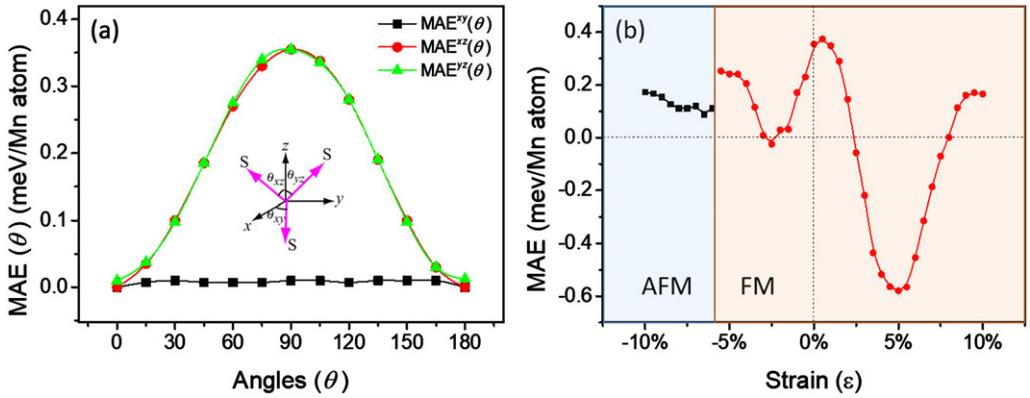

Figure 8. (a) Angular dependence of the MAE of 2D-$MnSe_2$ at 0% strain, with the direction lying on three different planes. (b) MAE of 2D-$MnSe_2$ under various strains.

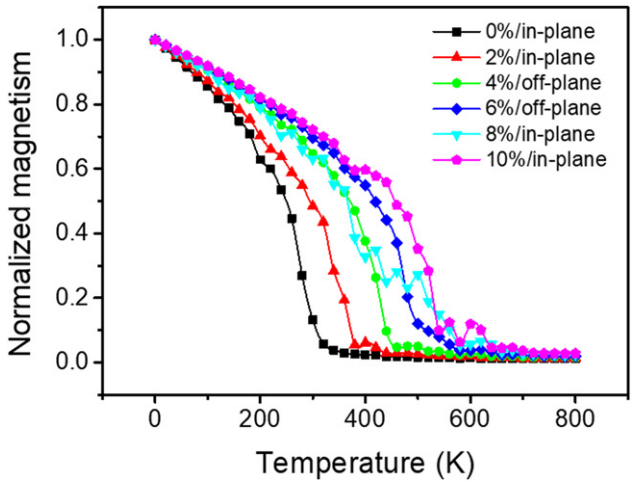

Figure 9. Curie temperature simulation of 2D-$MnSe_2$ under various tensile strains. Here percentage indicates the applied in-plain strain (denoted by different colours), followed by the preferred orientation of magnetic moments (in/off-plane), which flipped several times as the strain increases.

in this model, we consider the first, second and third nearest neighbour Heisenberg exchange integrations. The associated Heisenberg exchange integration parameters are J_1, J_2, and J_3, respectively. Firstly, this equation is treated in the classical approximation, and the spins S_i and S_j are described as dimensionless classical vectors of length S in the sphere ($S = 3/2$ for Mn^{4+}). To avoid and assess possible deviation while calculating J parameters. We adopt ($2 \times 4 \times 1$) 2D-$MnSe_2$ supercell and 17 possible non-equivalent magnetic configurations for our calculation. Furthermore, we keep the absolute value of the magnetic moment and geometric structure of various magnetic configurations the same. During the simulation, only the sign of the magnetic moments is changed. As depicted in figure 7(a), the energy of 2D-$MnSe_2$ calculated by DFT and predicted by Heisenberg model are illustrated. In these 17 configurations, the spin order of 2D-$MnSe_2$ transfers from AFM to FM, as illustrated in figure 7(a). To evaluate the deviation of the simulated parameter, we apply as follows:

$$\text{Deviation} = \frac{H^i_{\text{cal}} - H^i_{\text{fit}}}{H^{\max}_{\text{cal}}},$$

where H^i_{cal} is the ith magnetic interaction Hamiltonian determined by DFT, H^i_{fit} is the ith Hamiltonian by Heisenberg model and $H^{\max}_{\text{cal}}$ is the maximum Hamiltonian in these 17 configurations determined by DFT. As a transformation occurs when compressing 2D-$MnSe_2$, we define $H^{\max}_{\text{cal}}$ as $H^{\text{FM}}_{\text{cal}}$ when strain $> -6\%$, and define $H^{\max}_{\text{cal}}$ as $H^{\text{AFM}}_{\text{cal}}$ while strain $< -6\%$. Figure 7(b) presents the average deviations with error bars under various strains. The errors of this calculation are under the same level with the average deviation of 2.5%, which indicates relatively high accuracy of the simulation. The predicted parameters are shown in figure 7(c), it shows three Heisenberg exchange integrations. The first nearest neighbour parameter J_1 is with a large diving in the negative direction when tensile strain applied. Compressive strain, on the contrary, leads to a continuous increase of J_1 and changes its sign at the compressive strain of -4%. Although J_1 here changed from negative to positive, the strong spin frustration occurs at the compressive strain of -6%. Because the second and third interactions (J_2 and J_3) contribute a bit larger than first interaction (J_1) at -4% strain, thus maintaining the FM configuration of 2D-$MnSe_2$. The sign change of J is due to the competition of direct and through-bond interaction when compressing 2D-$MnSe_2$ as illustrated above.

We have further calculated its angular dependence of the magnetic anisotropy energy (MAE(θ)) of the system. figure 8(a) depicts the angular dependence of the MAE(θ) under 0% strain in the $xz-$, $yz-$, and $xy-$ planes. In the $xz-$ and $yz-$ plane, the energy strongly depends on the direction of magnetization, whereas in the $xy-$plane MAE^{xy} (θ) is about zero and irrelative with the direction of magnetization. Therefore, we regard $xy-$plane as a magnetic isotropic plane. We observe that single-layer 2D-$MnSe_2$ exhibits an easy magnetization axis parallel to the 2D plane of the material ($\theta = 0^\circ$, in-plane) and a hard magnetization axis perpendicular to the 2D plane ($\theta = 90^\circ$, off-plane). Therefore, we simply define the MAE of the system in $xy-$plane as 0, and MAE of $xz-$ and $yz-$ planes as:

$$\text{MAE} = E_{\text{off-plane}} - E_{\text{in-plane}},$$

where, $E_{\text{off-plane}}$ stands for the energy with off-plane magnetic torque, and $E_{\text{in-plane}}$ with in-plane magnetic torque. The Li and

Na adsorption would significantly decrease the MAE of 2D-$MnSe_2$ by about 0.16 meV per Mn atom (table S2), while the Mn vacancy would slightly enhance MAE by 0.03 meV per Mn atom (table S3). Figure 8(b) illustrates the MAE of 2D-$MnSe_2$ under various in-plane strains. It predicts four times of sign changes at around −3%, -2%, 2.5% and 8% strains, indicating four times of off- and in-plane magnetic configuration alterations.

High Curie temperature is often critical for a magnetic material. Tensile strain is proved to be a feasible and convenient method to improve the Curie temperature of materials. Thus we have evaluated the impact of tensile strain to its Curie temperature. Here we investigate it by atomistic spin model [38]. Since the value of J_1 is about 10 times greater than J_2 and J_3. Moreover, tensile strain further enlarges the gap between J_1 and J_2, J_3. To simplify the simulation, we only consider J_1 to estimate its Curie temperature. The result is shown in figure 9. When zero strain is applied, the calculated Curie temperature is 300 K, in line with previous theoretical [14] and experimental [6] studies. The Curie temperature would increase up to 530 K with the in-plane biaxial strain, indicating that the applied strain is efficient in enhancing the magnetic coupling of 2D-$MnSe_2$. Additionally, figure 9 presents fluctuations while 6% and 8% strains are applied. It can be ascribed to the sign changes of MAE energy around that strain ranges, in which a shift between in-plane and off-plane occurs.

4. Conclusions

To sum up, properties of 2D-$MnSe_2$ including band structure, DOS and magnetism have been investigated via first-principles calculations. A strain-induced phase transition from AFM metal to FM half metal, can be attributed to the competition between d–p–d through-bond interaction and d–d direct interaction. Charge doping is another method to tune the magnetic properties of 2D-$MnSe_2$, confirmed by practical adsorption and vacancies studies. The tensile strain can lead to a sharp increase in Curie temperature. Magnetic orientation flips between in- and off-plane are observed as strains applied. The 2D-$MnSe_2$ with tunable rich magnetic properties provides a great potential application for nanometer-scale magneto-elastic devices.

Data availability statement

All data that support the findings of this study are included within the article (and any supplementary files).

Conflict of interest

There are no conflicts to declare.

Acknowledgments

This work is financially supported by NSFC (Grant No. 12074126), the Foundation for Innovative Research Groups of the National Natural Science Foundation of China (Grant No. 51621001), the Fundamental Research Funds for the Central Universities (Grant No. 2020ZYGXZR076) and Natural Science Foundation of Guangdong Province of China (Grant No. 2016A030312011). The computer times at the National Supercomputing Centre in Guangzhou (NSCCGZ) are gratefully acknowledged.

ORCID iDs

Zhi-Wei Lu https://orcid.org/0000-0003-1661-9572
Xiao-Bao Yang https://orcid.org/0000-0001-8851-1988
Yu-Jun Zhao https://orcid.org/0000-0002-6923-1099

References

[1] Novoselov K S, Geim A K, Morozov S V, Jiang D, Zhang Y, Dubonos S V, Grigorieva I V and Firsov A A 2004 *Science* **306** 666–9
[2] Jasuja K, Ayinde K, Wilson C L, Behura S K, Ikenbbery M A, Moore D, Hohn K and Berry V 2018 *ACS Nano* **12** 9931–9
[3] Vaquero-Garzon L, Frisenda R and Castellanos-Gomez A 2019 *Nanoscale* **11** 12080–6
[4] Sun B, Zhu C-H, Liu Y, Wang C, Wan L-J and Wang D 2017 *Chem. Mater.* **29** 4367–74
[5] Castro Neto A H, Guinea F, Peres N M R, Novoselov K S and Geim A K 2009 *Rev. Mod. Phys.* **81** 109–62
[6] O'Hara D J *et al* 2018 *Nano Lett.* **18** 3125–31
[7] Tian Y, Gray M J, Ji H, Cava R J and Burch K S 2016 *2D Mater.* **3** 025035
[8] Huang B *et al* 2018 *Nat. Nanotechnol.* **13** 544–8
[9] Jiang S, Li L, Wang Z, Mak K F and Shan J 2018 *Nat. Nanotechnol.* **13** 549–53
[10] Zheng G *et al* 2020 *Phys. Rev. Lett.* **125** 047202
[11] Albarakati S *et al* 2019 *Sci. Adv.* **5** eaaw0409
[12] Lu Z-W, Qiu S-B, Xie W-Q, Yang X-B and Zhao Y-J 2020 *J. Appl. Phys.* **127** 033903
[13] Xu Q-F, Xie W-Q, Lu Z-W and Zhao Y-J 2020 *Phys. Lett.* A **384** 126754
[14] Kan M, Adhikari S and Sun Q 2014 *Phys. Chem. Chem. Phys.* **16** 4990
[15] Deng Y *et al* 2018 *Nature* **563** 94–9
[16] León-Brito N, Bauer E D, Ronning F, Thompson J D and Movshovich R 2016 *J. Appl. Phys.* **120** 083903
[17] Huang B *et al* 2017 *Nature* **546** 270–3
[18] Kan M, Zhou J, Sun Q, Kawazoe Y and Jena P 2013 *J. Phys. Chem. Lett.* **4** 3382–6
[19] Qian J and Lau S P 2018 *Mater. Today Energy* **10** 62–7
[20] Shang X *et al* 2019 *Int. J. Electrochem. Sci.* **14** 6000–8
[21] Cong C *et al* 2018 *Nano Res.* **11** 6227–36
[22] Gong Y *et al* 2015 *ACS Nano* **9** 11658–66
[23] Deng S, Hu H, Zhuang G, Zhong X and Wang J 2018 *Appl. Surf. Sci.* **441** 408–14
[24] Liu Z, Sorrell C C, Koshy P and Hart J N 2019 *ChemPhysChem* **20** 2074–81
[25] Avsar A, Ciarrocchi A, Pizzochero M, Unuchek D, Yazyev O V and Kis A 2019 *Nat. Nanotechnol.* **14** 674–8
[26] Hohenberg P and Kohn W 1964 *Phys. Rev.* **136** B864–71
[27] Kohn W and Sham L J 1965 *Phys. Rev.* **140** A1133–8
[28] Kresse G and Furthmüller J 1996 *Phys. Rev.* B **54** 11169
[29] Blöchl P E 1994 *Phys. Rev.* B **50** 17953–79
[30] Perdew J P, Burke K and Ernzerhof M 1996 *Phys. Rev. Lett.* **77** 3865–8
[31] Jain A, Hautier G, Moore C J, Ping Ong S, Fischer C C, Mueller T, Persson K A and Ceder G 2011 *Comput. Mater. Sci.* **50** 2295–310

[32] Wang L, Maxisch T and Ceder G 2006 *Phys. Rev.* B **73** 195107
[33] Heyd J, Scuseria G E and Ernzerhof M 2003 *J. Chem. Phys.* **118** 8207–15
[34] Heyd J, Scuseria G E and Ernzerhof M 2006 *J. Chem. Phys.* **124** 8207–15
[35] Slater J C 1951 *Phys. Rev.* **82** 538–41
[36] Monkhorst H J and Pack J D 1976 *Phys. Rev.* B **13** 5188–92
[37] Togo A and Tanaka I 2015 *Scr. Mater.* **108** 1–5
[38] Evans R F L, Fan W J, Chureemart P, Ostler T A, Ellis M O A and Chantrell R W 2014 *J. Phys.: Condens. Matter* **26** 103202
[39] Eren I, Iyikanat F and Sahin H 2019 *Phys. Chem. Chem. Phys.* **21** 16718–25
[40] Mondal P C and Fontanesi C 2017 *ChemPhysChem* **19** 60–6
[41] Jungwirth T, Sinova J, Manchon A, Marti X, Wunderlich J and Felser C 2018 *Nat. Phys.* **14** 200–3
[42] Li T 2012 *Phys. Rev.* B **85** 235407
[43] Azcatl A *et al* 2016 *Nano Lett.* **16** 5437–43
[44] Pan W *et al* 2012 *Sci. Rep.* **2** 893
[45] León A M, González J W, Mejía-López J, Crasto de Lima F and Suárez Morell E 2020 *2D Mater.* **7** 035008
[46] Webster L and Yan J A 2018 *Phys. Rev.* B **98** 144411
[47] Li Y, Li N, Zhao S, Fan J and Kai J-J 2020 *J. Mater. Chem.* A **8** 760–9
[48] Ma Y, Dai Y, Guo M, Niu C, Yu L and Huang B 2011 *Nanoscale* **3** 2301
[49] Kuc A, Zibouche N and Heine T 2011 *Phys. Rev.* B **83** 245213
[50] Zhou Y, Wang Z, Yang P, Zu X, Yang L, Sun X and Gao F 2012 *ACS Nano* **6** 9727–36
[51] Santos J, Marques M, Teles L and Ferreira L 2010 *Phys. Rev.* B **81** 115209
[52] Wu Z, Yu J and Yuan S 2019 *Phys. Chem. Chem. Phys.* **21** 7750–5
[53] Jang S W, Yoon H, Jeong M Y, Ryee S, Kim H-S and Han M J 2020 *Nanoscale* **12** 13501–6
[54] Gali S M, Pershin A, Lherbier A, Charlier J-C and Beljonne D 2020 *J. Phys. Chem.* C **124** 15076–84
[55] Singh D and Ahuja R 2019 *ACS Appl. Energy Mater.* **2** 6891–903